Chemical Science

ROYAL SOCIETY OF CHEMISTRY

EDGE ARTICLE

View Article Online
View Journal | View Issue

Cite this: *Chem. Sci.*, 2025, **16**, 10444

All publication charges for this article have been paid for by the Royal Society of Chemistry

Continuous coordination modulation with different heteroatoms unveils favorable single-atom Ni sites for near-unity CO selectivity in CO_2 electroreduction†

Shuangqun Chen,‡[a] Tong Cao,‡[a] Wen Yan,[b] Ke Zhao,[a] Yalin Guo,*[a] Tiantian Wu,*[c] Daliang Zhang,[a] Ming Ma,[b] Yu Han[d] and Jianfeng Huang*[a]

Coordination modulation is a key strategy for enhancing the catalytic activity of single-atom catalysts (SACs) in CO_2 electroreduction. However, achieving such modulation within the same framework by incorporating an array of heteroatoms with differing electronic properties remains unexplored, despite its potential for optimizing active sites. Here, we investigate unprecedentedly three Ni-based SACs (N_3Ni–C, N_3Ni–N, and N_3Ni–O), where varying coordinating atoms (C, N, and O) modulate continuously the electronic structure to explore their effects on CO_2 electroreduction. Compared to the N_3Ni–N catalyst with classic Ni–N_4 coordination, N_3Ni–C demonstrates significantly enhanced CO_2 conversion, achieving remarkably a near-unity Faradaic efficiency for CO (99.3%) at −0.7 V_{RHE} in the H-cell and a CO partial current density of 396.8 mA cm^{-2} at −1.15 V_{RHE} in the flow cell, whereas N_3Ni–O exhibits inferior performance. *Operando* and computational investigations reveal that both C- and O-coordination enhance CO_2 hydrogenation by elevating the Ni d-band center, thereby strengthening *COOH intermediate adsorption. However, the concurrent promotion of the hydrogen evolution reaction competes with CO_2 reduction, ultimately leading to opposite effects on performance. This work provides atomic-level insights into CO_2 electroreduction mechanisms and offers compelling strategies for improving SAC performance *via* coordination modulation with heteroatoms.

Received 13th March 2025
Accepted 2nd May 2025

DOI: 10.1039/d5sc01998b

rsc.li/chemical-science

1 Introduction

Rising global consumption of fossil fuels has led to excess CO_2 emissions, resulting in severe environmental repercussions and significant sustainability challenges.[1–4] The electrochemical CO_2 reduction reaction (eCO_2RR), powered by electrical energy preferably sourced from renewable origins, is recognized as a sustainable and clean approach for transforming CO_2 into valuable chemicals and fuels.[5–9] Carbon monoxide (CO), one of the simplest products of the eCO_2RR, enjoys strong market demand because of its versatility as a chemical feedstock extensively utilized in numerous industrial processes.[10–14] Thus, converting CO_2 to CO *via* electrochemical reduction offers a multifaceted solution that addresses environmental concerns, integrates renewable energy sources and supports industrial needs. However, this conversion is currently hindered by high overpotentials and competing reactions, such as the hydrogen evolution reaction (HER), necessitating the development of catalysts that are more efficient, selective, and ideally also cost-effective to enhance the practical viability of this process.[15–17]

Noble metals gold (Au) and silver (Ag) are widely regarded as the most efficient materials for catalyzing the conversion of CO_2 to CO in the eCO_2RR.[18–21] Nevertheless, their high costs and limited Faradaic efficiency (FE) at elevated current densities continue to present significant challenges.[22,23] To achieve efficient CO_2 conversion to CO, the rational design and controllable synthesis of electrocatalysts with improved reaction efficiency—grounded in a deep understanding of reaction mechanisms and structure–activity relationships—have emerged as key research areas. In this regard, single-atom catalysts (SACs) with metal–nitrogen–carbon (M–N–C) structures have attracted considerable attention in recent years for the eCO_2RR, owing to their low cost, well-defined atomic structures, and unique electronic properties.[24–27] SACs based on

[a]*State Key Laboratory of Coal Mine Disaster Dynamics and Control, Institute of Advanced Interdisciplinary Studies, School of Chemistry and Chemical Engineering, Chongqing University, Chongqing 400044, P. R. China. E-mail: guoyalin2022@cqu.edu.cn; jianfeng.huang@cqu.edu.cn*

[b]*School of Chemical Engineering and Technology, Xi'an Jiaotong University, Xi'an 710049, P. R. China*

[c]*School of Chemistry, Xi'an Jiaotong University, Xi'an 710049, P. R. China. E-mail: tianwu@xjtu.edu.cn*

[d]*Center for Electron Microscopy, South China University of Technology, Guangzhou 510640, P. R. China*

† Electronic supplementary information (ESI) available. See DOI: https://doi.org/10.1039/d5sc01998b

‡ These authors contributed equally to this work.

non-precious metals, such as Ni, Fe, Co, Mn, and Sn, have shown particular promise in the electrocatalytic conversion of CO_2 to CO.[28–32] Nevertheless, earlier studies of M–N–C SACs primarily employed symmetric $M–N_4$ coordination configurations, which, as a classic configuration, while demonstrating potential, typically require further improvement in electron transfer efficiency and the adsorption and activation of CO_2 molecules to enhance the overall efficiency of CO_2-to-CO conversion.[33–35] Furthermore, the reduction of CO_2 to CO typically involves two proton-coupled electron transfer steps, with overcoming the high energy barrier for the formation of the key intermediate COOH* in the first (rate-determining) step remaining a major challenge for $M–N_4$-configured SACs.[36,37] Given these challenges, research focused on modulating the electronic properties of the metallic active sites within M–N–C structures is crucial for achieving efficient CO_2 conversion.

Generally, N doping of carbon-based substrates induces significant changes in the properties of the support material, providing abundant coordination sites that facilitate the formation of various N-coordinated metal structures ($M–N_x$, $x \leq 4$).[38–41] As a result, beyond merely adjusting the number of N coordination sites, strategies have been developed to incorporate other heteroatoms with differing electronic properties—such as carbon (C) and boron (B), which possess electron-donating characteristics compared to N, and oxygen (O) and fluorine (F), which exhibit electron-withdrawing characteristics—into catalysts by substituting N atoms to optimize the electronic properties of the metallic active sites.[42–52] These approaches are particularly attractive because they effectively alter the charge distribution and/or structural symmetry of the active sites, providing significant opportunities to enhance the catalytic performance of M–N–C SACs. For example, the incorporation of electron-deficient C has been shown to enhance the catalytic performance of the eCO_2RR by modifying the electronic structure and thereby optimizing the binding energies of intermediates (*COOH and *CO) through cooperative regulation with N of the coordination environment of the Ni_2 center within the $N_x–Ni_2–C_{7-x}$ SACs.[53] In contrast, in $N_3–Sn–O_1$ SACs, the electron-rich nature of O atoms was found to precisely tune the binding strengths of intermediates (*COO and *COOH) in the eCO_2RR, markedly improving the selectivity for CO as the dominant product.[54]

Across reported results, heteroatoms, despite having opposite electronic effects relative to N (*i.e.*, electron-donating and electron-withdrawing), have all been shown to facilitate CO_2-to-CO conversion following N-coordination substitution. While this phenomenon is not unexpected, as relevant studies primarily employed only a single type of heteroatom to regulate the electronic properties of the active sites within different SAC systems, it raises confusion regarding which types of heteroatoms, based on their electronic effects, are more advantageous for CO_2-to-CO conversion in specific new SACs. Resolving this confusion is fundamentally important for a more comprehensive understanding of the structure–activity relationships and is also practically useful for the rational design of more advanced SACs aimed at efficient CO_2-to-CO conversion. To address this confusion, incorporating heteroatoms with opposite electronic effects into the coordination sites within the same SAC structure to enable bidirectional regulation of the electronic properties of metallic active centers is essential. However, to the best of our knowledge, no studies to date have investigated the regulation of active sites within the same SAC system by introducing different types of heteroatoms with varying electronic effects (*i.e.*, electronegativities stronger and weaker than N, thus presenting electron-donating and electron-withdrawing properties) for N-coordination substitution.

In this study, we report for the first time the selective replacement of a coordinated N atom in the $M–N_4$ structure with C and O atoms, respectively, to modulate continuously the coordination environment of the metallic sites in SACs and investigate their impacts on electrochemical CO_2-to-CO conversion. Due to their differing electronegativities and coordination properties, C and O atoms modify the electronic structure of the catalyst in distinct ways, enabling the identification of favorable active sites with optimal adsorption behaviors for intermediates in the eCO_2RR. To this end, we explore novel Ni-based SACs with three types of atomic coordination ($N_3Ni–C$, $N_3Ni–N$, and $N_3Ni–O$) supported on carbon nanoribbons. Among these catalysts, $N_3Ni–C$ demonstrates the best catalytic performance in the eCO_2RR, while $N_3Ni–O$ shows the worst. In more detail, for $N_3Ni–C$, the CO Faradaic efficiency (FE_{CO}) remains above 96.2% across a wide potential range from -0.6 to -1.0 V_{RHE}, reaching a maximum of 99.3% at -0.7 V_{RHE}, and is sustained for around 24 hours in an H-type cell. When applied in a flow cell, the $N_3Ni–C$ catalyst also exhibits a high FE_{CO} exceeding 98.6% at current densities ranging from 50 to 400 mA cm^{-2}. Detailed experimental characterization and theoretical density functional theory (DFT) calculations reveal that substituting the N-coordinate in the $N_3Ni–N$ catalyst with C promotes both CO_2 hydrogenation and the HER, with CO_2 hydrogenation being favored. In contrast, while the O-substitution also enhances both CO_2 hydrogenation and the HER, the HER is preferred over CO_2 hydrogenation. These contrasting preferences between the two competitive reactions lead to distinct CO_2 conversion performances, providing valuable insights into the favorable coordination environment for Ni sites to efficiently catalyze CO_2-to-CO conversion.

2 Results and discussion

2.1. Synthesis and characterization

Fig. 1a illustrates the synthesis of nickel-based SACs supported on carbon nanoribbons using a facile yet effective method involving physical mixing and high-temperature pyrolysis (see details in the ESI†). The process began with the preparation of a homogeneous precursor mixture by mixing and grinding ammonium chloride (NH_4Cl), nickel chloride hexahydrate ($NiCl_2 \cdot 6H_2O$), and rod-shaped perylene-3,4,9,10-tetracarboxylic dianhydride (PTCDA) powders (Fig. S1†), which serve as the sources of nitrogen (N), nickel (Ni), and carbon (C), respectively. The mixture was then calcined at high temperatures under an argon atmosphere, followed by post-treatment with sulfuric acid solution, yielding the final catalyst. Notably, the catalyst structure was determined by the pyrolysis temperature, with

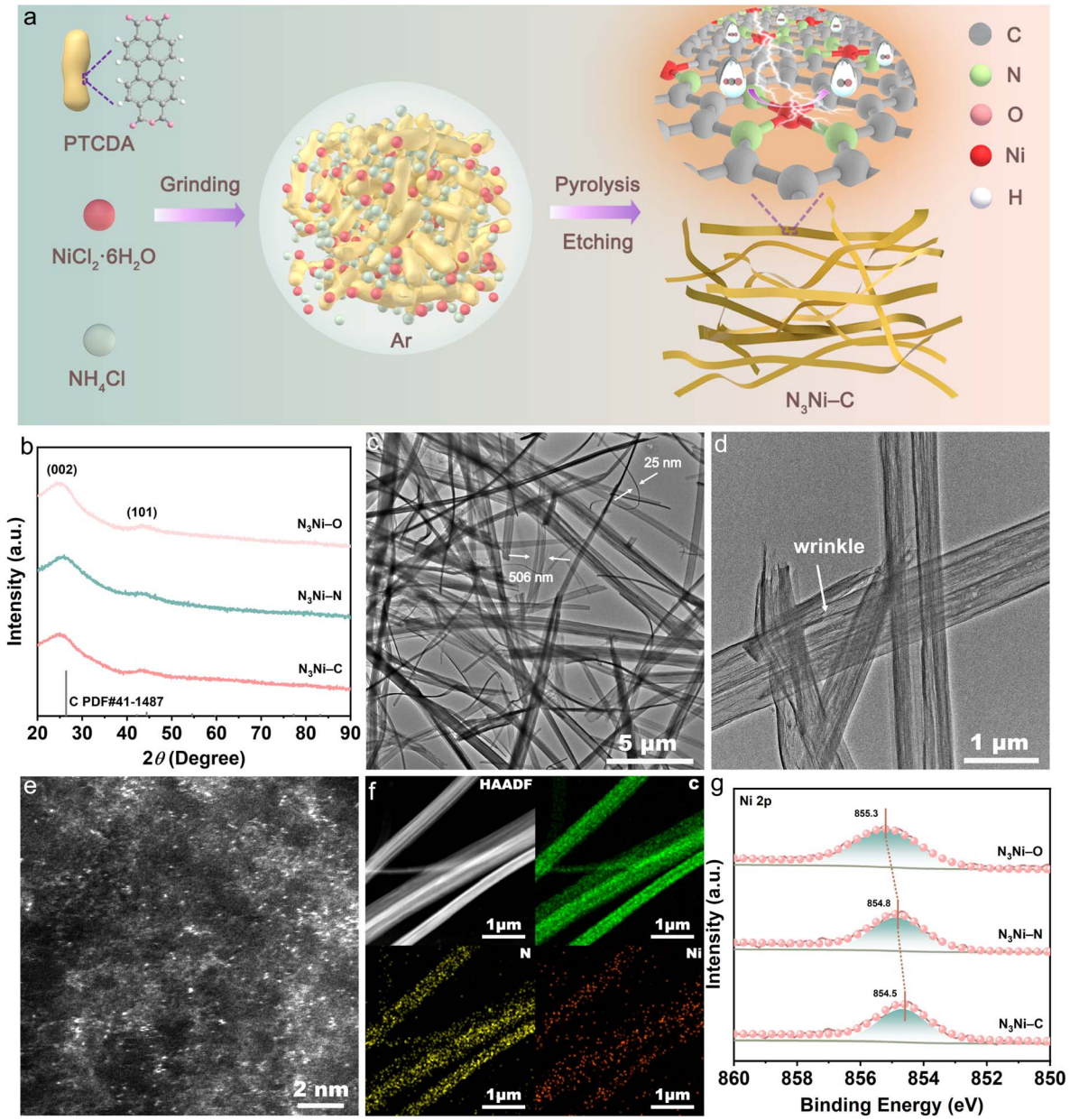

Fig. 1 Preparation and structural characterization of $N_3Ni–C/N/O$. (a) Schematic illustration of the synthesis pathway for $N_3Ni–C$. (b) XRD patterns. (c) and (d) Low- (c) and high- (d) magnification TEM images. (e) AC-HAADF-STEM image. (f) HAADF-STEM and elemental mapping images. (g) XPS spectra of Ni $2p_{3/2}$.

$N_3Ni–O$, $N_3Ni–N$, and $N_3Ni–C$ forming at 800 °C, 900 °C, and 1000 °C, respectively. This temperature-dependent structural evolution among $N_3Ni–O$, $N_3Ni–N$, and $N_3Ni–C$ likely arises from the varying thermal stability of O, N, and C during high-temperature treatment, governed by their respective binding strengths with the central Ni atom (O < N < C). This results in differing volatilization tendencies (O > N > C) as the annealing temperature increases—a phenomenon that has been well-documented.[22] However, the underlying mechanism may be more intricate, potentially involving factors such as the formation of unsaturated metal sites, partial reduction of the catalyst, or other temperature-induced transformations, as suggested in previous studies.[1] To gain a deeper understanding of the growth mechanism, each individual component was removed from the precursor mixture to examine its effect on the product, while keeping all other synthesis procedures unchanged. Experimental results showed that the absence of $NiCl_2 \cdot 6H_2O$ resulted in irregular carbon nitride (CN) thin layers (Fig. S2†). When NH_4Cl was removed, only nickel (Ni) nanoparticles were observed, with the carbon material completely volatilized at high temperatures. Similarly, after removing PTCDA, NH_4Cl completely decomposed as well, leaving only Ni nanoparticles. These results indicate that the nitrogen from NH_4Cl plays a critical role in stabilizing the carbon material at high

temperatures, while the presence of nickel from $NiCl_2 \cdot 6H_2O$ is essential for maintaining the nanoribbon structure.

X-ray diffraction (XRD) was first employed to analyze the phase and structural information of the three samples (*i.e.*, N_3Ni–O, N_3Ni–N, and N_3Ni–C). As shown in Fig. 1b, two broad diffraction peaks appeared at approximately 26° and 44° in all samples, corresponding to the (002) and (101) planes of graphite carbon, respectively. No diffraction peaks related to Ni crystallites were observed, indicating that the Ni species were either too small in size or too low in loading.[25,30] The graphitic carbon structure of the samples was further confirmed by Raman spectroscopy, which revealed two characteristic bands typical of carbon materials: one assigned to disordered carbon (1355 cm^{-1}, I_D) and the other to graphitic carbon (1585 cm^{-1}, I_G) (Fig. S3†). Notably, the I_D/I_G ratio was 1.000, 0.907, and 0.886 for N_3Ni–O, N_3Ni–N and N_3Ni–C, respectively, indicating a gradual decrease in the disorder of the carbon substrate with increasing pyrolysis temperature.[24,37] The decreasing disorder can be attributed to the increased volatilization of heteroatoms (such as O or N) from the carbon substrate induced by higher temperatures, contributing to a more ordered carbon structure.

Fig. 1c presents a representative transmission electron microscopy (TEM) image of the N_3Ni–C sample, illustrating its nanoribbon morphology with thickness and width approximately 25 nm and 500 nm, respectively. Such a one-dimensional structure is expected to facilitate oriented electron transport and promote the exposure of surface-active sites, thereby enhancing electrocatalytic activity.[55] Higher-magnification TEM imaging further revealed the presence of thin-layered wrinkles and micropores on the ribbons (Fig. 1d and e), which can potentially increase the surface area of the material. Indeed, the N_3Ni–C sample achieved a Brunauer–Emmett–Teller (BET) surface area of 114.11 $m^2\ g^{-1}$, the highest among the three samples studied (Fig. S4†). We further examined the atomic structure of N_3Ni–C using aberration-corrected high-angle annular dark-field scanning transmission electron microscopy (AC-HAADF-STEM). The AC-HAADF-STEM image depicts bright dots sharply against a dim substrate due to the stark Z-contrast between Ni atoms and the carbon substrate, which unambiguously suggests the presence of Ni species in the form of highly dispersed single atoms (Fig. 1e). Elemental mapping confirmed that C, N, and Ni elements were uniformly distributed across the carbon support (Fig. 1f). Taken together, the TEM findings are in good alignment with the XRD and Raman results discussed earlier, providing evidence for the single-atomic-Ni structure of the N_3Ni–C sample. Likewise, N_3Ni–O and N_3Ni–N possess analogous single-atom structures, as verified by TEM and elemental mapping (Fig. S5 and S6†). Inductively coupled plasma optical emission spectrometry (ICP-OES) determined the Ni loading for the three samples to be 0.774 wt%, 0.393 wt%, and 0.375 wt%, respectively, indicating a slight decrease in Ni content with increasing pyrolysis temperature.

The chemical states of Ni species were investigated using X-ray photoelectron spectroscopy (XPS) (Fig. 1g). The Ni 2p spectra revealed that the principal Ni $2p_{3/2}$ peaks for the three samples (N_3Ni–O, N_3Ni–N, and N_3Ni–C) were all positioned between the Ni^0 peak (853.5 eV) and the Ni^{2+} peak (855.8 eV), suggesting their oxidation states ranging between 0 and +2. Notably, as the electronegativity of the coordinating atoms (O, N, and C) decreased, the Ni $2p_{3/2}$ peaks of the respective samples (N_3Ni–O, N_3Ni–N, and N_3Ni–C) shifted progressively to lower binding energies, specifically, from 855.3 eV to 854.5 eV.

This trend highlights the electronic interactions between the central Ni atom and the surrounding coordinating atoms, which affect the electron density around the Ni center and alter its electronic environment.

The chemical state and local atomic environment of Ni species within the three samples were further analyzed using X-ray absorption spectroscopy (XAS), with Ni foil, NiO, and nickel phthalocyanine (NiPc) serving as references. Consistent with the XPS results (Fig. 1g), the X-ray absorption near-edge structure (XANES) spectra (Fig. 2a) show that the absorption edges of N_3Ni–O, N_3Ni–N, N_3Ni–C and NiPc are all positioned between those of Ni foil and NiO, confirming their positive valence states lying between Ni^0 and Ni^{2+}. Likewise, as the coordinating atom varies from O to N to C, the absorption edge of the corresponding sample gradually approaches that of Ni foil, demonstrating a shift toward a lower valence state. To gain further insights into the local coordination characteristics of Ni atoms, we conducted an analysis using extended X-ray absorption fine structure (EXAFS) spectroscopy at the Ni K-edges. The Fourier-transformed k^3-weighted EXAFS (FT-EXAFS) spectra are presented in Fig. 2b, along with their curve-fitting analysis and results shown in Fig. 2c–e, S7 and Table S1.† As illustrated in the FT-EXAFS spectra, prominent characteristic peaks corresponding to Ni–N, Ni–Ni, and Ni–O coordination were observed at approximately 1.90, 2.48, and 2.07 Å for NiPc, Ni foil, and NiO, respectively. These reference peaks provide a solid basis for comparison with the Ni SAC samples (Fig. 2b and Table S1†). Notably, the Ni–Ni coordination peak was absent in all three Ni SAC samples, which agrees well with the AC-HAADF-STEM results indicating that the Ni species exist as isolated single atoms rather than as Ni particles. Furthermore, all Ni SAC samples exhibited the Ni–N coordination peak, although with a slight shift in peak position. The curve-fitting analysis further revealed that the prominent peak in the N_3Ni–N sample arises from the collective scattering of four Ni–N bonds with a bond length of 1.88 Å, confirming a $Ni–N_4$ coordination environment (Fig. 2d, and Table S1†). In contrast, the central Ni atom in the N_3Ni–C sample coordinates with three N atoms (bond length: 1.88 Å) and one C atom (bond length: 2.11 Å), resulting in a N_3–Ni–C coordination (Fig. 2c and Table S1†). Similarly, in the N_3Ni–O sample, the Ni atom coordinates with three N atoms (bond length: 1.91 Å) and one O atom (bond length: 2.10 Å), forming a N_3–Ni–O coordination (Fig. 2e and Table S1†), with the O atom bonded to the C matrix (Fig. S16†). Additionally, the fitting results were corroborated by density functional theory (DFT) calculations using structural models based on the fitted coordination environments (Fig. S17†). These calculations indicate that the Ni atom exhibits increasingly higher oxidation states as one coordinating atom changes from C to N to O (Fig. 2f–h), which echoes the afore-discussed XPS results (Fig. 1g).

To intuitively visualize the coordination characteristics of these samples, we performed wavelet transform (WT) analysis on the k^3-

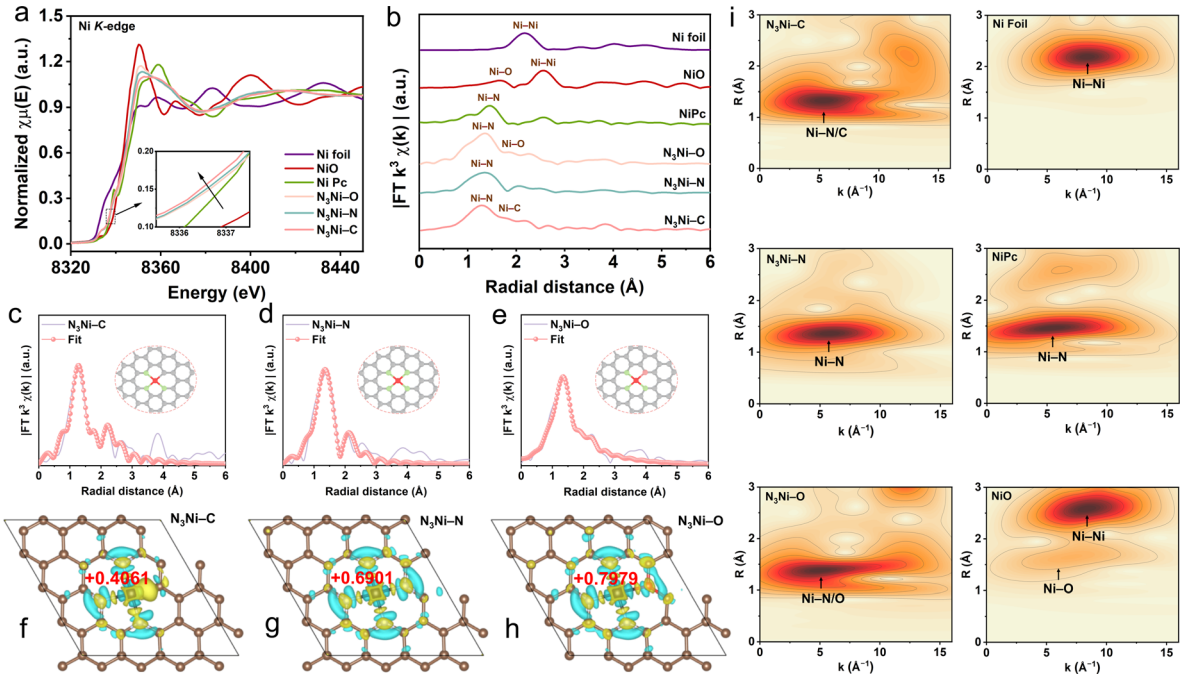

Fig. 2 XAS-analysis of N_3Ni–C/N/O and reference samples. (a) and (b) Ni K-edge XANES spectra (a) and FT-EXAFS spectra (b) for N_3Ni–C, N_3Ni–N, N_3Ni–O, and reference samples (Ni foil, NiPc, and NiO). (c–e) Experimental and fitted FT-EXAFS curves for N_3Ni–C, N_3Ni–N, and N_3Ni–O, with insets showing the local coordination structure of the Ni center. (f)–(h) Charge density difference and Bader charge analysis for N_3Ni–C, N_3Ni–N, and N_3Ni–O. (i) Wavelet transform (WT) EXAFS patterns for N_3Ni–C, N_3Ni–N, N_3Ni–O and references samples (Ni foil, NiPc, and NiO).

weighted EXAFS data of the Ni K-edges. The resulting scattering intensity distribution patterns in *K*, *R*-space are displayed in Fig. 2i. Specifically, all three Ni SAC samples display their scattering intensity maxima at coordinates similar to those observed in the intensity distribution pattern of NiPc. This similarity is expected, as Ni–N coordination predominantly contributes to the scattering intensity in the Ni SAC samples. In addition to confirming the presence of the Ni–N bond, this similarity also rules out the existence of Ni–Ni bonds, thereby reaffirming the atomic dispersion of the Ni species in the three Ni SAC samples. Another interesting observation is that the scattering intensity pattern of the N_3Ni–N sample displays similar symmetry to that of NiPc, whereas the N_3Ni–C and N_3Ni–O samples exhibit obvious asymmetries. The differing pattern symmetries among the three Ni SAC samples highlight the role of C/O atoms in disrupting the centrosymmetry of the Ni–N_4 coordination upon substituting one N atom. Collectively, the XAS results demonstrate a bidirectional modulation of the electronic structure of Ni SACs by engineering coordination atoms (*i.e.*, C and O) that have lower and higher electronegativities, respectively, compared to the N atom within the same coordination framework. This strategy provides a versatile platform for exploring optimized single-atom sites for the electrochemical conversion of CO_2 to CO.

2.2. Performance for the eCO_2RR

The electrocatalytic CO_2RR performance for the three Ni SACs was evaluated, in comparison to a Ni-free CN substrate, in both neutral and alkaline electrolytes using a three-electrode H-type electrolysis cell and a flow cell, respectively. Initially, linear sweep voltammetry (LSV) was performed in the H-cell containing a CO_2-saturated 0.5 M $KHCO_3$ solution (pH = 7.0). The results revealed that the N_3Ni–C catalyst exhibits the lowest onset potential and the highest current responses among the catalysts studied, indicating its superior electrocatalytic activity (Fig. 3a). Further investigation demonstrated that the high activity of N_3Ni–C is directly related to the CO_2RR, as evidenced by significantly lower current responses of the same catalyst in an Ar-saturated $KHCO_3$ solution (Fig. S8†).

Building upon these findings, controlled potentials ranging from −0.5 to −1.0 V_{RHE} were applied to investigate the potential-dependent distribution of CO_2RR products, including both gaseous and liquid species, which were quantitatively analyzed using online gas chromatography and ^1H nuclear magnetic resonance (NMR) spectroscopy, respectively. This potential range was selected because all catalysts showed a surge in cathodic current density starting around −0.5 V_{RHE} (Fig. 3a). At all applied potentials, only H_2 and CO were detected, with the total Faradaic efficiency (FE) approaching 100% (Fig. 3b and S9†). Remarkably, the N_3Ni–C catalyst achieved exceptional CO selectivity exceeding 96.2% across a broad potential window (−0.6 to −1.0 V_{RHE}), outperforming N_3Ni–N, N_3Ni–O, and CN, throughout the entire investigated potential range (−0.5 to −1.0 V_{RHE}). In particular, a near-unity FE_{CO} of 99.3% was achieved at a low potential of −0.7 V_{RHE} for N_3Ni–C. This performance not only significantly surpasses the optimal performances of N_3Ni–N (94.5% at −0.7 V_{RHE}), N_3Ni–O (90.4% at −0.8 V_{RHE}), and CN (58.5% at −0.7 V_{RHE}) but also positions N_3Ni–C among the best Ni-based SACs reported to date for the electrochemical CO_2 conversion to CO (Fig. 3c and Table S2†).

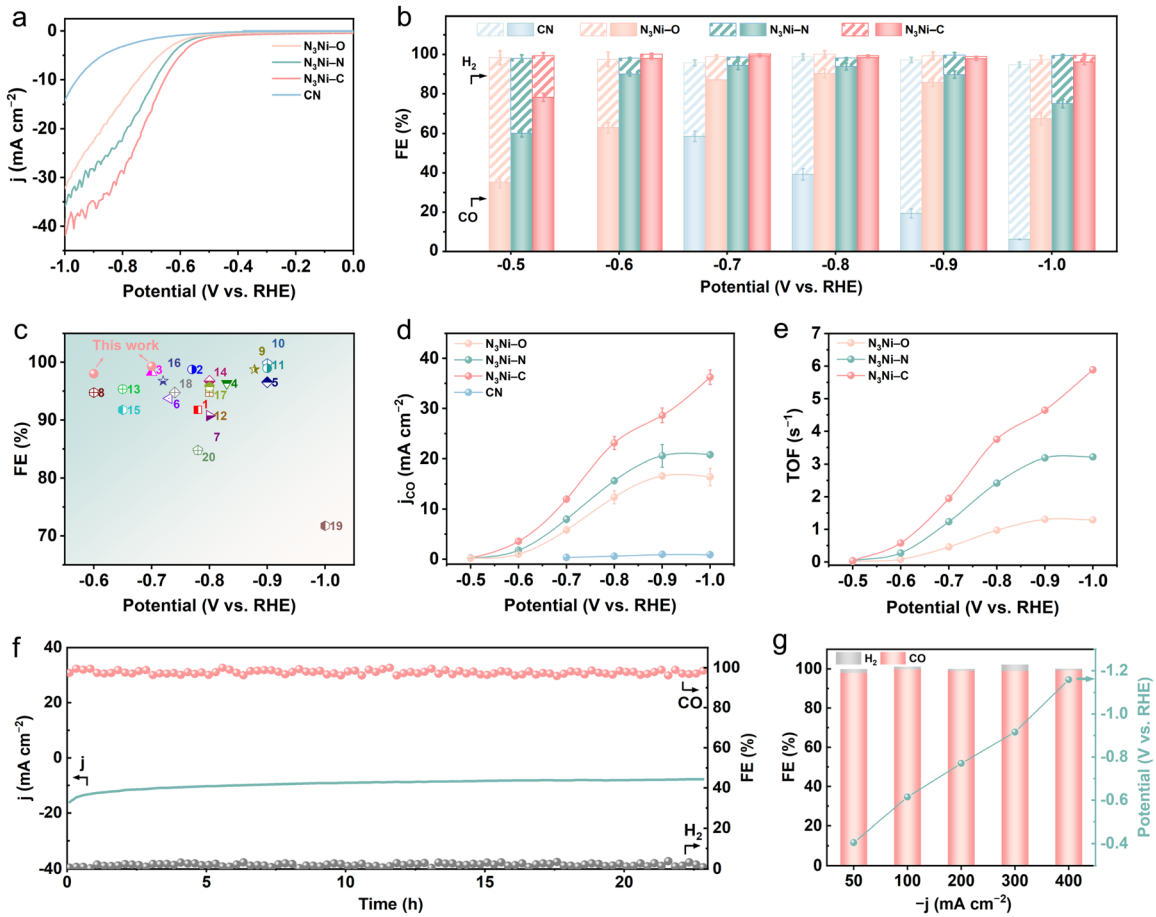

Fig. 3 The eCO$_2$RR performance of N_3Ni–C/N/O and comparative samples. (a) LSV curves. (b) Faradaic efficiency (FE) for CO and H_2. (c) Comparison of the FEs at specific potentials for N_3Ni–C and other reported Ni SACs (Table S2†). (d) Partial current density of CO. (e) Turnover frequency (TOF). (f) eCO$_2$RR stability test for N_3Ni–C in an H-cell at −0.7 V_{RHE}. (g) eCO$_2$RR performance of N_3Ni–C on a gas diffusion layer electrode in a flow cell configuration.

Moreover, with the same catalyst loading, the N_3Ni–C catalyst demonstrated significantly higher geometric total current density (j) and CO partial current density (j_{CO}) compared to the other catalysts at each individual potential (Fig. 3d, and S10†). However, because the catalysts have different Ni loadings, the intrinsic eCO$_2$RR activity, expressed as the turnover frequency (TOF) for CO, was further calculated by normalizing the number of Ni atoms in each catalyst (see calculation details in the ESI†). As shown in Fig. 3e, the N_3Ni–C catalyst exhibits higher TOF than N_3Ni–N and N_3Ni–O at all tested potentials, reaching up to 5.89 s^{-1} at −1.0 V_{RHE}. This performance is comparable to the best-performing Ni-based SACs reported in the literature (Table S2†). The TOF comparison strongly demonstrates the favorable effect of the unique N_3–Ni–C coordination in delivering high intrinsic activity for CO_2-to-CO conversion. Consistently, N_3Ni–C exhibited the lowest Tafel slope among the tested samples (Fig. S11†). Additionally, the double-layer capacitance (C_{dl}), obtained *via* cyclic voltammetry in a non-Faradaic region (Fig. S12†), indicates that N_3Ni–C has a slightly larger value (13.0 mF cm^{-2}) compared to N_3Ni–N (12.7 mF cm^{-2}) and N_3Ni–O (11.0 mF cm^{-2}). The overall high C_{dl} for all three samples is likely attributable to the ribbon-like carbon support, which offers a high surface area for exposing single-atomic active sites (see BET results discussed earlier). Therefore, the superior catalytic activity of N_3Ni–C can be attributed to the greater exposure of active sites with higher intrinsic activity.

Importantly, the N_3Ni–C catalyst retained its outstanding performance around 24 hours of electrolysis at −0.7 V_{RHE} (Fig. 3f). After the durability test, the current density was largely retained, and the FE_{CO} changed negligibly. Post-mortem characterization of N_3Ni–C (including XRD, TEM, elemental analysis, and AC-HAADF-STEM images) also revealed trivial changes in phase, composition, morphology, and atom dispersion, demonstrating its excellent structural stability (Fig. S13–S15†). Furthermore, when assembled in a flow electrolyzer equipped with a gas diffusion electrode (GDE), N_3Ni–C achieved a high FE_{CO} of over 98.6% at various industrially relevant current densities (50–400 mA cm^{-2}) and reached a current density of up to 400 mA cm^{-2} (equivalent to a CO partial current density of 396.8 mA cm^{-2}) at −1.15 V_{RHE}, surpassing most state-of-the-art CO-selective catalysts (Fig. 3g and Table S3†). These stability-test results and flow-cell performance collectively demonstrate the potential industrial feasibility of the N_3Ni–C catalyst for CO production *via* the eCO$_2$RR.

2.3. Mechanistic investigation through *operando* ATR-SEIRAS measurements and DFT calculations

Based on the above results, it is concluded that, compared to N_3Ni–N, substituting a nitrogen atom with carbon—an element with lower electronegativity than nitrogen—enhances the electrochemical conversion of CO_2 to CO (Fig. 3a, b, d, e and S10–S12†). Conversely, substitution with oxygen, which has higher electronegativity than nitrogen, has an adverse effect. These contrasting impacts, arising from the differing electronegativities of carbon and oxygen relative to nitrogen, motivate us to investigate the underlying mechanism.

We first conducted *operando* attenuated total reflection surface-enhanced infrared absorption spectroscopy (ATR-SEIRAS) measurements to monitor surface-adsorbed reaction intermediates during the CO_2RR on the most active N_3Ni–C catalyst. These measurements were implemented in both Ar- and CO_2-saturated 0.5 M $KHCO_3$ solutions, over a potential range from the open circuit potential (OCP) to −1.1 V_{RHE} (Fig. 4a and b). At the OCP, the spectra were featureless, indicating that no intermediates were adsorbed on the catalyst surface. However, as the potential was decreased to −0.3 V_{RHE} and further to −1.1 V_{RHE}, multiple vibrational bands emerged. Two peaks at approximately 1387 cm^{-1} and 1258 cm^{-1} were observed, corresponding to carbonate species, CO_3^{2-} and HCO_3^-, respectively, while a peak at 1647 cm^{-1} was attributed to adsorbed water ($*H_2O$).[56,57] Notably, in the CO_2-saturated solution, the intensity of the $*H_2O$ peak gradually decreased with increasingly negative potentials, indicating accelerated consumption of $*H_2O$. In contrast, the $*H_2O$ peak in the Ar-saturated system remained nearly unchanged. This difference in the behavior of $*H_2O$ suggests that, as the potential becomes more negative, CO_2 reacts more rapidly with the $*H_2O$. The enhanced CO_2 reduction at more negative potentials is further evidenced by the noticeable weakening of the HCO_3^- peak (~1260 cm^{-1}), as CO_2 consumption depletes locally the HCO_3^- concentration (Fig. 4b). Moreover, the reduction of CO_2 is accompanied by the appearance of a new peak at 1443 cm^{-1} (Fig. 4b), which corresponds to the *COOH intermediate—a well-documented critical precursor for CO formation in the CO_2RR.[58,59] The intensity of this peak increased significantly with more negative potentials, whereas it was absent in the Ar-saturated system irrespective of the potential applied (Fig. 4a). Furthermore, no signals for adsorbed CO (*CO) were detected, which is attributable to the weak adsorption and rapid desorption of CO on the N_3Ni–C surface.[60,61] Overall, the ATR-SEIRAS results indicate that the N_3Ni–C coordination structure facilitates the formation of the *COOH intermediate while promoting the rapid desorption of CO. These findings help explain the high catalytic activity and exceptional CO selectivity observed for the CO_2RR over the N_3Ni–C catalyst.

With insights gained from *operando* ATR-SEIRAS measurements, we conducted DFT computations to examine the CO_2-to-CO conversion *via* the *COOH intermediate and the parasitic HER across the three Ni SACs. Model optimization results indicate that CO_2 reduction preferentially occurs at the Ni center for all three catalysts (Fig. S18†). By comparison, the HER is favored at the Ni center for N_3Ni–C and N_3Ni–N, but shifts to the neighboring carbon site of the substrate in N_3Ni–O. The free energy profiles (Fig. 4c) reveal that the N_3Ni–N structure exhibits a relatively high energy barrier (0.71 eV) for the CO_2

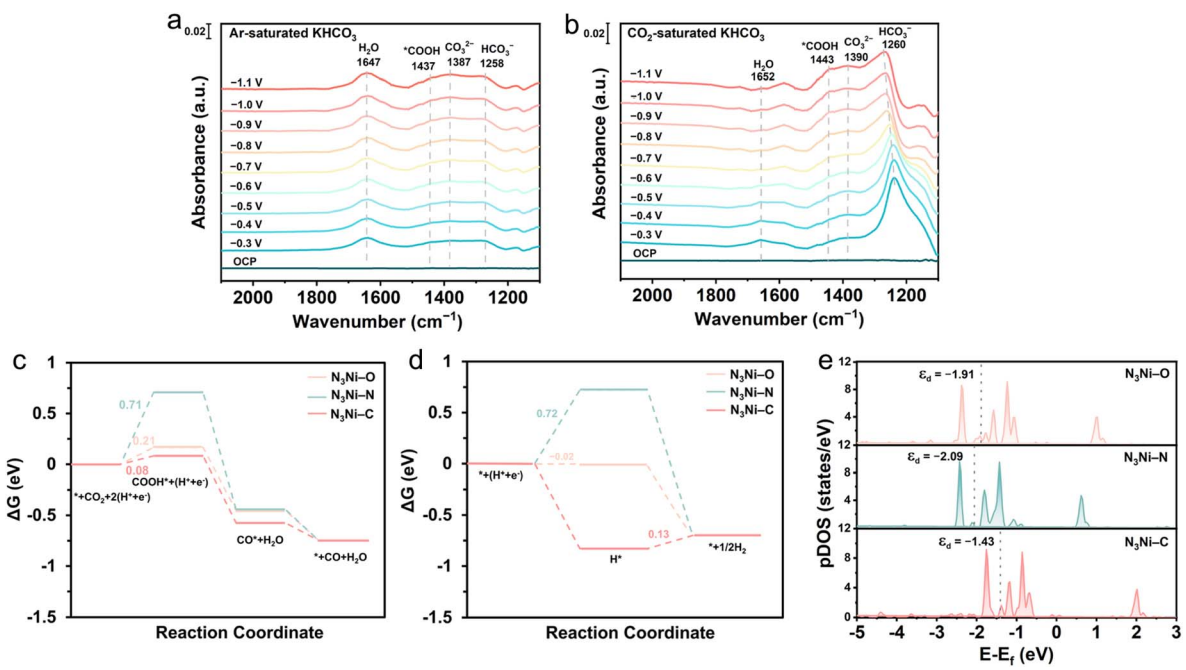

Fig. 4 Investigation of CO_2-to-CO conversion mechanisms. (a) and (b) *operando* ATR-SEIRAS of N_3Ni–C recorded at various applied potentials in an Ar-saturated (a) and CO_2-saturated (b) 0.5 M $KHCO_3$ solution. (c) and (d) free energy diagrams for the eCO_2RR to CO (c) and HER (d) on N_3Ni–C, N_3Ni–N, and N_3Ni–O. (e) Projected density of states (pDOS) of the Ni 3d orbital in N_3Ni–C, N_3Ni–N, and N_3Ni–O, with the d band center (ε_d) labeled.

hydrogenation step (CO_2 → *COOH), the rate-determining step (RDS) in the CO_2-to-CO conversion. This high energy barrier is consistent with previous reports,[38,41] attributed to the high degree of symmetry in N_3Ni–N. In contrast, the N_3Ni–C structure displays a significantly lower energy barrier (0.08 eV) for the CO_2 hydrogenation step, which explains its higher CO_2 conversion activity observed experimentally. When the competitive HER is considered (Fig. 4d), the N_3Ni–C catalyst needs to overcome an energy barrier of 0.13 eV for H_2 production. This value exceeds the energy requirement (0.08 eV) for the CO_2 hydrogenation step, providing a clear account for the exceptional CO selectivity exhibited by the N_3Ni–C catalyst. For N_3Ni–O, the energy barrier for the CO_2 hydrogenation step (0.21 eV) is also remarkably reduced compared to that of N_3Ni–N. Theoretically, this lower energy barrier should translate to higher CO production activity. However, experimental observations contradict this expectation, as N_3Ni–O demonstrates lower activity than N_3Ni–N (Fig. 3a, b, d and e). A deeper analysis, incorporating the HER, reveals that N_3Ni–O favors the HER pathway over CO_2 conversion, with energy barriers of −0.02 eV and 0.21 eV, respectively. By contrast, N_3Ni–N shows a slight preference for CO_2 conversion (0.71 eV) over the HER (0.72 eV). This difference explains why N_3Ni–O underperforms compared to N_3Ni–N in CO formation, despite its reduced energy barrier for the CO_2 hydrogenation step. Further support for the observed catalytic preferences is provided by the calculated differences between the thermodynamic limiting potentials for the CO_2RR and HER, defined as $\Delta U_L = U_L(CO_2) – U_L(H_2)$. The ΔU_L values for N_3Ni–C, N_3Ni–N, and N_3Ni–O are −0.05, −0.01, and 0.23 V (Fig. S19†), respectively, which align well with the trends in selectivity discussed above.

Taken together, these results illustrate that substituting the N-coordination with C or O atoms disrupts the symmetry of the Ni–N_4 structure in N_3Ni–N, leading to a significantly reduced energy barrier for the CO_2 hydrogenation step. Projected density of states (pDOS) calculations (Fig. 4e) further attribute this reduction to the elevated d-band center (ε_d) of the Ni sites (N_3Ni–N: −2.09 eV; N_3Ni–O: −1.91 eV; N_3Ni–C: −1.43 eV), which enhances *COOH adsorption, as evidenced by the adsorption energies of the *COOH intermediate on the three catalysts (Fig. S19†) and the corresponding charge density difference (Fig. S20†). Meanwhile, C/O substitution also substantially lowers the energy barrier for the HER. However, the contrasting extents to which C and O substitutions influence CO_2 conversion and the HER ultimately result in C substitution favoring CO_2 conversion over the HER, while O substitution does the opposite.

3 Conclusions

In summary, we have successfully fabricated a series of carbon-nanoribbon-supported Ni SACs (namely, N_3Ni–C, N_3Ni–N, and N_3Ni–O) where one coordinating atom varies across C, N, and O. This series has been designed to investigate how coordination modulation affects the performance of electrochemical CO_2 reduction, with the goal of identifying the optimal coordination environment to enhance the efficiency of Ni sites. *Operando* characterization and DFT calculations reveal that both C and O coordination beneficially modulate the energy barriers for CO_2 hydrogenation and the HER, albeit to different extents. This modulation disparity results in a preference for CO_2 conversion over the HER on N_3Ni–C, while the HER is favored over CO_2 conversion on N_3Ni–O. Consequently, compared to the N_3Ni–N catalyst with the conventional Ni–N_4 structure, the N_3Ni–C catalyst demonstrates significantly enhanced CO_2 conversion performance, with the FE_{CO} exceeding 96.2% over a broad potential range (−0.6 to −1.0 V_{RHE}) and peaking at 99.3% at −0.7 V_{RHE} in the H-cell. Moreover, the CO partial current density reaches an impressive 396.8 mA cm^{-2} at −1.15 V_{RHE} in the flow cell, establishing N_3Ni–C as a leading contender among state-of-the-art CO_2-to-CO conversion catalysts. This study highlights the potential of tuning the competition between CO_2 conversion and the HER through strategic coordination modulation, providing a novel perspective for designing and developing highly efficient SACs for CO_2 electroreduction to CO.

Data availability

All relevant data for this article are provided in the main text and the ESI.†

Author contributions

Shuangqun Chen: conceptualization, methodology, data curation and analysis, writing (original draft). Tong Cao: data curation, data analysis. Wen Yan: methodology, data analysis. Ke Zhao: methodology, data analysis. Yalin Guo: data analysis, writing-review & editing, funding acquisition. Tiantian Wu: formal analysis, software development, writing-original draft, writing-review & editing. Daliang Zhang: data analysis, supervision. Ming Ma: data analysis, supervision. Yu Han: data analysis, writing-review & editing. Jianfeng Huang: conceptualization, data analysis, funding acquisition, investigation, project administration, resources, supervision, writing-review & editing.

Conflicts of interest

There are no conflicts to declare.

Acknowledgements

This work was supported by the National Key Research and Development Project of China (No. 2022YFE0113800), Thousand Talents Program for Distinguished Young Scholars, the China Postdoctoral Science Foundation (2023M740396), the National Natural Science Foundation of China (22308036), and the Postdoctoral Innovation Talents Support Program of Chongqing (CQBX202320). T. W. acknowledges the financial support from the Fundamental Research Funds for the Central Universities (xzy012024052). Supercomputing facilities were provided by Hefei Advanced Computing Center and Computing Center in Xi'an. Dr Lirong Zheng from the Institute of High Energy Physics, Chinese Academy of Sciences, is gratefully

acknowledged for his invaluable assistance with the XAS measurements.

Notes and references

1 M. Li, H. Wang, W. Luo, P. C. Sherrell, J. Chen and J. Yang, *Adv. Mater.*, 2020, **32**, 2001848.
2 J. Huang, M. Mensi, E. Oveisi, V. Mantella and R. Buonsanti, *J. Am. Chem. Soc.*, 2019, **141**, 2490–2499.
3 B. Zhang, L. Wang, D. Li, Z. Li, R. Bu and Y. Lu, *Chem Catal.*, 2022, **2**, 3395–3429.
4 J. Ding, H. Yang, X. Ma, S. Liu, W. Liu, Q. Mao, Y. Huang, J. Li, T. Zhang and B. Liu, *Nat. Energy*, 2023, **8**, 1386–1394.
5 Z. Xu, R. Lu, Z.-Y. Lin, W. Wu, H.-J. Tsai, Q. Lu, Y. C. Li, S.-F. Hung, C. Song, J. C. Yu, Z. Wang and Y. Wang, *Nat. Energy*, 2024, **8**, 1397–1406.
6 J. Huang, T. Yang, K. Zhao, S. Chen, Q. Huang and Y. Han, *J. Energy Chem.*, 2021, **62**, 71–102.
7 Z. Lyu, S. Zhu, M. Xie, Y. Zhang, Z. Chen, R. Chen, M. Tian, M. Chi, M. Shao and Y. Xia, *Angew. Chem., Int. Ed.*, 2020, **60**, 1909–1915.
8 S. Kong, X. Lv, X. Wang, Z. Liu, Z. Li, B. Jia, D. Sun, C. Yang, L. Liu, A. Guan, J. Wang, G. Zheng and F. Huang, *Nat. Catal.*, 2022, **6**, 6–15.
9 Y. Cai, R. Yang, J. Fu, Z. Li, L. Xie, K. Li, Y.-C. Chang, S. Ding, Z. Lyu, J.-R. Zhang, J.-J. Zhu, Y. Lin and W. Zhu, *Nat. Synth.*, 2024, **3**, 891–902.
10 J. d. Yi, X. Gao, H. Zhou, W. Chen and Y. Wu, *Angew. Chem., Int. Ed.*, 2022, **61**, e202212329.
11 Q. Hao, H. Zhong, J. Wang, K. Liu, J. Yan, Z. Ren, N. Zhou, X. Zhao, H. Zhang, D. Liu, X. Liu, L. Chen, J. Luo and X. Zhang, *Nat. Synth.*, 2022, **1**, 719–728.
12 Y. Chen, J. Wei, M. S. Duyar, V. V. Ordomsky, A. Y. Khodakov and J. Liu, *Chem. Soc. Rev.*, 2021, **50**, 2337–2366.
13 R. Zhao, Y. Wang, G. Ji, J. Zhong, F. Zhang, M. Chen, S. Tong, P. Wang, Z. Wu, B. Han and Z. Liu, *Adv. Mater.*, 2022, **35**, 2205262.
14 Y. Xu, X. Zhang, C. Yang, C. Gong, X. Qin, H. Sun, H. Chen, M. A. Soldatov, K. Zheng, C. Li, T. Gan, J. Li, J. He and Q. Liu, *Adv. Energy Mater.*, 2024, **14**, 2400143.
15 S. Nitopi, E. Bertheussen, S. B. Scott, X. Liu, A. K. Engstfeld, S. Horch, B. Seger, I. E. L. Stephens, K. Chan, C. Hahn, J. K. Nørskov, T. F. Jaramillo and I. Chorkendorff, *Chem. Rev.*, 2019, **119**, 7610–7672.
16 S. Ma, M. Sadakiyo, M. Heima, R. Luo, R. T. Haasch, J. I. Gold, M. Yamauchi and P. J. A. Kenis, *J. Am. Chem. Soc.*, 2016, **139**, 47–50.
17 B. Wang, M. Wang, Z. Fan, C. Ma, S. Xi, L. Y. Chang, M. Zhang, N. Ling, Z. Mi, S. Chen, W. R. Leow, J. Zhang, D. Wang and Y. Lum, *Nat. Commun.*, 2024, **15**, 1719.
18 W. Zhu, R. Michalsky, Ö. Metin, H. Lv, S. Guo, C. J. Wright, X. Sun, A. A. Peterson and S. Sun, *J. Am. Chem. Soc.*, 2013, **135**, 16833–16836.
19 Y. Chen, C. W. Li and M. W. Kanan, *J. Am. Chem. Soc.*, 2012, **134**, 19969–19972.
20 M. Ma, K. Liu, J. Shen, R. Kas and W. A. Smith, *ACS Energy Lett.*, 2018, **3**, 1301–1306.
21 S. Liu, S. Wu, M. Gao, M. Li, X. Fu and J. Luo, *ACS Sustain. Chem. Eng.*, 2019, **7**, 14443–14450.
22 Y. Li, N. M. Adli, W. Shan, M. Wang, M. J. Zachman, S. Hwang, H. Tabassum, S. Karakalos, Z. Feng, G. Wang, Y. C. Li and G. Wu, *Energy Environ. Sci.*, 2022, **15**, 2108–2119.
23 G. Jun, C. Hsu, L. B. Bai, H. Chen and X. Hu, *Science*, 2019, **364**, 1091–1094.
24 D. Yao, C. Tang, X. Zhi, B. Johannessen, A. Slattery, S. Chern and S. Z. Qiao, *Adv. Mater.*, 2023, **35**, 2209386.
25 C. Wang, X. Wang, H. Ren, Y. Zhang, X. Zhou, J. Wang, Q. Guan, Y. Liu and W. Li, *Nat. Commun.*, 2023, **14**, 5108.
26 X. Wang, N. Fu, J.-C. Liu, K. Yu, Z. Li, Z. Xu, X. Liang, P. Zhu, C. Ye, A. Zhou, A. Li, L. Zheng, L.-M. Liu, C. Chen, D. Wang, Q. Peng and Y. Li, *J. Am. Chem. Soc.*, 2022, **144**, 23223–23229.
27 W. Xia, Y. Xie, S. Jia, S. Han, R. Qi, T. Chen, X. Xing, T. Yao, D. Zhou, X. Dong, J. Zhai, J. Li, J. He, D. Jiang, Y. Yamauchi, M. He, H. Wu and B. Han, *J. Am. Chem. Soc.*, 2023, **145**, 17253–17264.
28 X. Hai, S. Xi, S. Mitchell, K. Harrath, H. Xu, D. F. Akl, D. Kong, J. Li, Z. Li, T. Sun, H. Yang, Y. Cui, C. Su, X. Zhao, J. Li, J. Pérez-Ramírez and J. Lu, *Nat. Nanotechnol.*, 2021, **17**, 174–181.
29 C. Liu, Y. Wu, K. Sun, J. Fang, A. Huang, Y. Pan, W.-C. Cheong, Z. Zhuang, Z. Zhuang, Q. Yuan, H. L. Xin, C. Zhang, J. Zhang, H. Xiao, C. Chen and Y. Li, *Chem*, 2021, **7**, 1297–1307.
30 J. Liang, H. Zhang, Q. Song, Z. Liu, J. Xia, B. Yan, X. Meng, Z. Jiang, X. W. Lou and C. S. Lee, *Adv. Mater.*, 2023, **36**, 2303287.
31 M. Wang, Y. Yao, Y. Tian, Y. Yuan, L. Wang, F. Yang, J. Ren, X. Hu, F. Wu, S. Zhang, J. Wu and J. Lu, *Adv. Mater.*, 2023, **35**, 2210658.
32 X. Zu, X. Li, W. Liu, Y. Sun, J. Xu, T. Yao, W. Yan, S. Gao, C. Wang, S. Wei and Y. Xie, *Adv. Mater.*, 2019, **31**, 1808135.
33 X. Li, S. Han, W. Wu, K. Zhang, B. Chen, S. Zhou, D. Ma, W. Wei, X. Wu, R. Zou and Q. Zhu, *Energy Environ. Sci.*, 2023, **16**, 502–512.
34 C. Lv, K. Huang, Y. Fan, J. Xu, C. Lian, H. Jiang, Y. Zhang, C. Ma, W. Qiao, J. Wang and L. Ling, *Nano Energy*, 2023, **111**, 108384.
35 C. Hu, Y. Zhang, A. Hu, Y. Wang, X. Wei, K. Shen, L. Chen and Y. Li, *Adv. Mater.*, 2023, **35**, 2209298.
36 Z. Zeng, L. Y. Gan, H. Bin Yang, X. Su, J. Gao, W. Liu, H. Matsumoto, J. Gong, J. Zhang, W. Cai, Z. Zhang, Y. Yan, B. Liu and P. Chen, *Nat. Commun.*, 2021, **12**, 4088.
37 X. Chen, W. Liu, Y. Sun, T. Tan, C. X. Du and Y. Li, *Small Methods*, 2023, **7**, 2201311.
38 Y. Zhou, Q. Zhou, H. Liu, W. Xu, Z. Wang, S. Qiao, H. Ding, D. Chen, J. Zhu, Z. Qi, X. Wu, Q. He and L. Song, *Nat. Commun.*, 2023, **14**, 3776.
39 S. Gong, W. Wang, R. Lu, M. Zhu, H. Wang, Y. Zhang, J. Xie, C. Wu, J. Liu, M. Li, S. Shao, G. Zhu and X. Lv, *Appl. Catal., B*, 2022, **318**, 121813.
40 Y. Li, X. Lu, S. Xi, D. Luan, X. Wang and X. Lou, *Angew. Chem., Int. Ed.*, 2022, **61**, e202201491.
41 C. Li, W. Ju, S. Vijay, J. Timoshenko, K. Mou, D. A. Cullen, J. Yang, X. Wang, P. Pachfule, S. Brückner, H. S. Jeon,

F. T. Haase, S. C. Tsang, C. Rettenmaier, K. Chan, B. R. Cuenya, A. Thomas and P. Strasser, *Angew. Chem., Int. Ed.*, 2022, **61**, e202114707.
42 Y. Deng, J. Zhao, S. Wang, R. Chen, J. Ding, H.-J. Tsai, W.-J. Zeng, S.-F. Hung, W. Xu, J. Wang, F. Jaouen, X. Li, Y. Huang and B. Liu, *J. Am. Chem. Soc.*, 2023, **145**, 7242–7251.
43 X. Zhao, S. Huang, Z. Chen, C. Lu, S. Han, C. Ke, J. Zhu, J. Zhang, D. Tranca and X. Zhuang, *Carbon*, 2021, **178**, 488–496.
44 S. Chen, X. Li, C. W. Kao, T. Luo, K. Chen, J. Fu, C. Ma, H. Li, M. Li, T. S. Chan and M. Liu, *Angew. Chem., Int. Ed.*, 2022, **61**, e202206233.
45 X. Wang, Y. Wang, X. Sang, W. Zheng, S. Zhang, L. Shuai, B. Yang, Z. Li, J. Chen, L. Lei, N. M. Adli, M. K. H. Leung, M. Qiu, G. Wu and Y. Hou, *Angew. Chem., Int. Ed.*, 2021, **60**, 4192–4198.
46 K. Li, S. Zhang, X. Zhang, S. Liu, H. Jiang, T. Jiang, C. Shen, Y. Yu and W. Chen, *Nano Lett.*, 2022, **22**, 1557–1565.
47 Y. N. Gong, L. Jiao, Y. Qian, C. Y. Pan, L. Zheng, X. Cai, B. Liu, S. H. Yu and H. L. Jiang, *Angew. Chem., Int. Ed.*, 2020, **59**, 2705–2709.
48 G. Guan, Y. Liu, F. Li, X. Shi, L. Liu, T. Wang, X. Xu, M. Zhao, J. Ding and H. B. Yang, *Adv. Funct. Mater.*, 2024, **34**, 2408111.
49 T. Zheng, K. Jiang, N. Ta, Y. Hu, J. Zeng, J. Liu and H. Wang, *Joule*, 2019, **3**, 265–278.
50 P. Song, B. Hu, D. Zhao, J. Fu, X. Su, W. Feng, K. Yu, S. Liu, J. Zhang and C. Chen, *ACS Nano*, 2023, **17**, 4619–4628.
51 Y. Wang, P. Zhu, R. Wang, K. C. Matthews, M. Xie, M. Wang, C. Qiu, Y. Liu, H. Zhou, J. H. Warner, Y. Liu, H. Wang and G. Yu, *ACS Nano*, 2024, **18**, 26751–26758.
52 L. Zong, K. Fan, L. Cui, F. Lu, P. Liu, B. Li, S. Feng and L. Wang, *Angew. Chem., Int. Ed.*, 2023, **62**, e202309784.
53 Y. N. Gong, C. Y. Cao, W. J. Shi, J. H. Zhang, J. H. Deng, T. B. Lu and D. C. Zhong, *Angew. Chem., Int. Ed.*, 2022, **61**, e202215187.
54 J. Guo, W. Zhang, L. H. Zhang, D. Chen, J. Zhan, X. Wang, N. R. Shiju and F. Yu, *Adv. Sci.*, 2021, **8**, 2102884.
55 Y. Li, J. Chen, S. Chen, X. Liao, T. Zhao, F. Cheng and H. Wang, *ACS Energy Lett.*, 2022, **7**, 1454–1461.
56 M. Huang, B. Deng, X. Zhao, Z. Zhang, F. Li, K. Li, Z. Cui, L. Kong, J. Lu, F. Dong, L. Zhang and P. Chen, *ACS Nano*, 2022, **16**, 2110–2119.
57 L. Zhang, J. Feng, S. Liu, X. Tan, L. Wu, S. Jia, L. Xu, X. Ma, X. Song, J. Ma, X. Sun and B. Han, *Adv. Mater.*, 2023, **35**, 202209590.
58 J. Huang and R. Buonsanti, *Chem. Mater.*, 2018, **31**, 13–25.
59 B. Chen, D. Shi, R. Deng, X. Xu, W. Liu, Y. Wei, Z. Liu, S. Zhong, J. Huang and Y. Yu, *ACS Catal.*, 2024, **14**, 16224–16233.
60 M. Dunwell, Q. Lu, J. M. Heyes, J. Rosen, J. G. Chen, Y. Yan, F. Jiao and B. Xu, *J. Am. Chem. Soc.*, 2017, **139**, 3774–3783.
61 Z. Chen, C. Wang, X. Zhong, H. Lei, J. Li, Y. Ji, C. Liu, M. Ding, Y. Dai, X. Li, T. Zheng, Q. Jiang, H. Peng and C. Xia, *Nano Lett.*, 2023, **23**, 7046–7053.